Adaptive Knee Joint Exoskeleton Based on Biological Geometries

Donghai Wang, Kok-Meng Lee, *Fellow, IEEE*, Jiajie Guo, *Member, IEEE*, and Can-Jun Yang

***Abstract*—This paper presents a relatively complete analytical model of a knee joint interacting with a two-link exoskeleton for investigating the effects of different exoskeleton designs on the internal joint forces/torque in the knee. The closed kinematic chain formed by the leg and exoskeleton has a significant effect on the joint forces/torque in the knee. A bio-joint model is used to capture this effect by relaxing a commonly made assumption that approximates a knee joint as a perfect engineering pin-joint in designing an exoskeleton. Based on the knowledge of a knee-joint kinematics, an adaptive knee-joint exoskeleton has been designed to eliminate negative effects associated with the closed leg-exoskeleton kinematic chain on a human knee. For experimental validation, the flexion motion of an artificial human knee is investigated comparing the performances of five exoskeleton designs against the case with no exoskeleton. Analytical results that estimate internal forces/torque using the kinematic and dynamic models (based on the properties of a knee joint) agree well with data obtained experimentally. This investigation illustrates the applications of the analytical model for designing an adaptive exoskeleton that minimizes internal joint forces due to a knee-exoskeleton interaction.**

***Index Terms*—Adaptive exoskeleton, closed-chain mechanism, knee-exoskeleton model, knee-joint forces/torque, knee-joint rolling/sliding.**

NOMENCLATURE

Capitalized symbols

C	Instantaneous contact point; **R** Rotational transformation.
C_o	Contact point without sliding; S_p pure rolling distance.
C_p	Cam profile; S_r rolling distance.
E	Attaching point; S_s sliding distance.
J	Lower-leg moment-of-inertia; **V***i* tangential vector at point *i*.
O	Lower-leg mass-center; *X, Y* reference frame.
P	Position in *XY* coordinates.

Lowercase symbols

a	Scaling factor; f_l contact force in cam roller.
d_i	Cam torque moment arm; f_m motor force.
f_d	Cam slider force; f_r, f_θ knee force in r and θ directions.
f_{er}, $f_{e\theta}$	Force along and normal to link; k_r, k_θ compliance in r and θ directions.
ℓ	Human lower-leg length; $r_a r$ value based on C' location.
ℓ_E	Initial lower-link length; r_m measured r value.
ℓ_i	Deviation distance; $r_{\rm maj}$, $r_{\rm min}$ ellipse major and minor radii.
m	Lower-leg mass; r_l, r_s calibrated and fitted r values.
o	Initial attachment point; s cam-shape factor.
$\boldsymbol{p}$	Position in xy coordinates; u end slider displacement.
r	Lower-leg mass-center; x, y moving coordinate frame.

Greek letter symbols

α	Deviation angle; ρ curvature radius.
γ	Adjoint deviation angle; τ_a knee active torque.
δ	Knee end angle τ_e interactive torque.
ε	Force angle in cam slot τ_f friction torque.
η	Force angle in motor; τ_g lower-leg gravity torque.
θ	Lower-leg flexion angle; τ_l cam roller torque.
θ_E	Torque angle; τ_m motor torque.
μ	Slider friction coefficient; φ lower link flexion angle.

Subscripts

E	For point E; i initial state or value.
e	For exoskeleton; O for point O.

Manuscript received February 1, 2013; revised May 20, 2013; accepted July 23, 2013. Date of publication September 6, 2013; date of current version April 25, 2014. Recommended by Technical Editor M. Iwasaki. This work was supported in part by the Science Fund for Creative Research Groups of the National Natural Science Foundation of China under Grant 51221004 and in part by the National Key Technology R&D Program of the National Science and Technology Ministry under Grant 2009BAI71B03.

D. Wang and C.-J. Yang are with the State Key Laboratory of Fluid Power Transmission and Control, Zhejiang University, Hangzhou 310027, China (e-mail: 06jxlwdh@zju.edu.cn; ycj@zju.edu.cn).

K.-M. Lee is with the George W. Woodruff School of Mechanical Engineering, Georgia Institute of Technology, Atlanta, GA 30332–0405, USA, and also with Huazhong University of Science and Technology, Wuhan 430074, China (e-mail: kokmeng.lee@me.gatech.edu).

J. Guo is with the State Key Laboratory of Digital Manufacturing Equipment and Technology, School of Mechanical Science and Engineering, Huazhong University of Science and Technology, Wuhan 430074, China (e-mail: jiajie.guo@hust.edu.cn).

Color versions of one or more of the figures in this paper are available online at http://ieeexplore.ieee.org.

Digital Object Identifier 10.1109/TMECH.2013.2278207

I. INTRODUCTION

EXOSKELETONS have been widely studied in mechatronics and robotics for rehabilitating and assisting human body motions. Applications include an adaptive wearable ankle robot for the treatments of ankle sprain through physical rehabilitation [1], a wearable multiphalanges device for post-stroke rehabilitation [2], a cable-driven arm exoskeleton [3], and an active leg exoskeleton [4] facilitating stroke patients neuromotor training gait to improve their functional walking ability. Although exoskeletons or orthosis can assist or adjust human musculoskeletal system, there are potentials for discomfort and injuries if it is not adaptive to the wearer. To reduce any

negative effect from a rigid exoskeleton on a human biological joint (bio-joint), physical forces/torque acting on the human bio-joints must be well understood.

Exoskeleton designs are often based on assumptions that simplify bio-joints to engineering joints to reduce kinematic complexity to a tractable form. For example, knee-joints are commonly modeled as a pin-joint which has only one DOF [5] with a fixed rotation axis. However, knee-joints have a nonuniform geometry with varying articulating surfaces, and a nonconstant rotation axis. In the crossed four-bar linkage model [6], the knee geometry is defined to consist of anterior cruciate ligament (ACL), posterior cruciate ligament (PCL), femur, and tibia. A 3-D analytical model taking into account the knee-joint surface geometry can be found in [7]. For standardization in a clinical joint coordination system, the knee joint is described with six DOFs [8]. When designing a lower-extremity exoskeleton joint, the natural knee kinematics must be considered.

The human knee instrumented with a two-link mechanism forms a closed kinematic loop. Unlike the case of an open kinematic chain (such as human walking with no exoskeleton) experiencing no impulse within the joint, a combined knee-exoskeleton tends to create a residual force if the DOFs of the exoskeleton are insufficient to compromise with that of a human joint to align the motion axis or any human–machine kinematic differences [9]–[13]. Although some ergonomic (passive or self-adjusting) joints [14], [15] are designed, an analytical model considering a bio-joint and the effect of exoskeleton on a human joint have not been well understood. Considering the knee joint with two DOFs (rotation and translation), the closed kinematic chain experiences a singularity when the knee is fully extended introducing an impulsive knee force internally [16]. The design of a lower-extremity exoskeleton with insufficient knee-motion knowledge can disturb and even damage a human knee; thus, the bio-joint kinematics should be fully accounted for in exoskeleton designs.

Human knee kinematics has been widely analyzed by researchers with an interest to understand abrasion (or the effect of femur rolling or sliding on tibia). Due to human knee closure and complexity, traditional off-the-shelf sensors cannot be implanted directly in the joint capsule, which have led to the development of noninvasive, high-resolution MRI-assisted technology [17], [18] that facilitates interpreting the behavior of a knee joint [16]. This paper further extends the kinematic and dynamic models formulated in [19] for analyzing misalignments of the rotational axes in a knee-exoskeleton structure, so that the negative effects of exoskeleton on the knee joint can be effectively eliminated.

The remainder of this paper is organized as follows.

1) This paper begins with a relatively complete analytical model describing the kinematics and dynamics of a knee-exoskeleton (K-E) structure for investigating the effects of exoskeleton designs on a knee joint.
2) Methods for calibrating dominant physical parameters that characterize the rolling/sliding contact conditions in the knee are presented, which are essential for solving the solutions to the kinematics and dynamics of a K–E structure. For the purposes of validating the analytical models, the flexion of an artificial human knee joint was investigated for comparing the performances of different exoskeleton designs against the case without an exoskeleton.
3) The analytical models and calibration method are validated by comparing results against published data and experimental data measured on an existing lower extremity rehabilitation exoskeleton (LERE) [20] which was modified to accommodate natural motions of a typical human knee.
4) Five different kinematic configurations are analyzed both numerically and experimentally to illustrate the effects of exoskeleton designs on the internal forces/torque within a human knee; the investigation has led to the design of an adaptive exoskeleton.

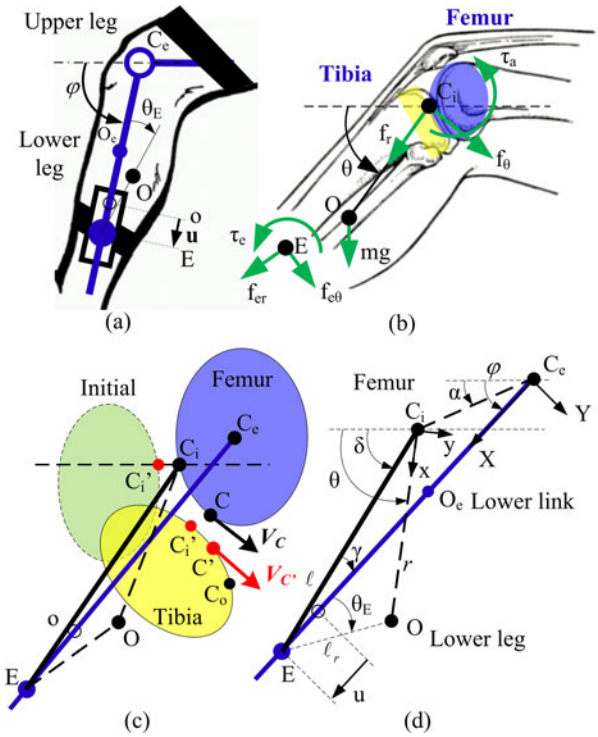

Fig. 1. Knee-exoskeleton kinematic and dynamic models. (a) K-E mechanism. (b) Kinetic parameters in polar coordinates. (c) Rolling/sliding contact. (d) Kinematic parameters.

II. Analytical Knee–Exoskeleton (K-E) Models

Fig. 1 shows a typical K-E structure with the upper link and leg held stationary at a horizontal position while the knee flexes (angle θ) under gravity. As shown in Fig. 1(a), the lower link rotates (angle φ) about the pin joint C_e, and slides (displacement u) relative to the attaching point E fixed on the lower leg; and u is defined to be zero at $\theta = 0$, so that the point "o" on the lower link overlaps with E.

Using a lumped-parameter approach in polar coordinate (r, θ) with origin at C_i, the motion of the lower leg (mass m, moment of inertia J) can be described by the displacement of its mass-center O as shown in Fig. 1(b), where τ_e is the actuating torque of the exoskeleton; $(f_{er}, f_{e\theta})$ are the forces exerted by the exoskeleton at E (along and perpendicular to the lower link);

$(f_r,\ f_\theta)$ and τ_a denote the internal forces/torque exerted by the femur on the tibia in the knee, respectively; and τ_g is the torque due to the gravitational force *mg* (or the weight) of the lower leg. For investigating the effects of exoskeleton designs on a knee, the relative motion of the lower link (m_e, J_e) to the lower leg is characterized by the displacement u of the mass-center O_e and the angle θ_E between EO_e and *EO*.

Fig. 1(c) shows a separated bio-joint coupled with a exoskeleton link C_eE, where C_i and C_i' are initial contact points on the femur and tibia, respectively, C and C' are instantaneous contact points, and C_o is instantaneous contact point when joint rolls purely. As the lower leg flexes ($\theta > 0$), the tibia rolls and slides on the femur. The instantaneous rotation axis of the knee moves with the tibia as illustrated in Fig. 1(c). Because C_i and C_e are nonconcentric, the line-vector $\mathbf{P}_i(C_i \text{ to } E)$ and its orientation δ change as geometrically shown in Fig. 1(d).

It is desired that the K-E bio-mechatronic structure with constant u and θ_E displacements while the lower leg flexes, and that the user experiences minimum internal forces/torque (f_r, f_θ, τ_a). To minimize the kinematic deviations and hence the internal forces and torque in the knee, the displacement between C_e and E on the exoskeleton must be made adaptable in design.

A. Kinematics

To facilitate the following discussions, the reference coordinate system *XY* is assigned at C_e on the exoskeleton with its X-axis pointing along the lower link as shown in Fig. 1(d); and the coordinate system *xy* at C_i on the femur with its x-axis pointing toward the centroid of the lower leg. The coordinate transformation from *xy* to *XY* frames is given by (1) where l_i is the distance between C_i and C_e:

$$\mathbf{P} = [\mathbf{R}(z, \theta - \varphi)]\mathbf{p} + \mathbf{P}_i \tag{1}$$

where

$$[\mathbf{R}(z, \theta - \varphi)] = \begin{bmatrix} \cos(\theta - \varphi) & -\sin(\theta - \varphi) \\ \sin(\theta - \varphi) & \cos(\theta - \varphi) \end{bmatrix} \quad \text{and}$$

$$\mathbf{P}_i = \begin{bmatrix} X_i \\ Y_i \end{bmatrix} = \begin{bmatrix} \ell_i \cos(\varphi - \alpha) \\ -\ell_i \sin(\varphi - \alpha) \end{bmatrix}.$$

For a given design, $\mathbf{P}_i$ (or the location C_i) is calibrated as will be described in Section III and thus ℓ_i and α are assumed known.

1) Forward kinematics: Given the angular displacement φ of the exoskeleton, the forward kinematics of the knee-exoskeleton mechanism solves for the knee angle $\theta(\varphi)$, the displacement $u(\varphi)$, and the torque angle $\theta_E(\varphi)$ in terms of the calibrated contact point C_i for a specified geometry (O, E, C_e, ℓ and ℓ_E):

$$\mathbf{P}_E = \begin{bmatrix} \ell_E + u \\ 0 \end{bmatrix} = \begin{bmatrix} \ell\cos(\delta - \varphi) + \ell_i \cos(\varphi - \alpha) \\ \ell\sin(\delta - \varphi) - \ell_i \sin(\varphi - \alpha) \end{bmatrix} \tag{2a}$$

$$\mathbf{P}_O = \begin{bmatrix} X_O \\ Y_O \end{bmatrix} = \begin{bmatrix} r\cos(\theta - \varphi) + \ell_i \cos(\varphi - \alpha) \\ r\sin(\theta - \varphi) - \ell_i \sin(\varphi - \alpha) \end{bmatrix} \tag{2b}$$

$$r = |\mathbf{P}_O - \mathbf{P}_{Ci}|. \tag{2c}$$

The knee flexion angle can be derived from (2b)

$$\theta(\varphi) = \cos^{-1}\left(\frac{X_O - \ell_i \cos(\varphi - \alpha)}{r}\right) + \varphi. \tag{3}$$

Using the cosine law for the triangle ΔC_iEC_e in Fig. 1(d),

$$u(\varphi) = \sqrt{\ell^2 + \ell_i^2 - 2\ell\ell_i \cos(\pi - \delta + \alpha)} - \ell_E \tag{4}$$

where $\ell = \ell_i \frac{\sin(\varphi - \alpha)}{\sin(\delta - \varphi)}$. Similarly, using the sine law for ΔC_iEO in Fig. 1(d),

$$\theta_E(\varphi) = \sin^{-1}\left(\frac{r\sin(\theta - \varphi - \gamma)}{|\mathbf{P}_E - \mathbf{P}_O|}\right) - \gamma \tag{5}$$

where

$$\gamma = \delta - \varphi = \sin^{-1}\left(\frac{\ell_i}{\ell}\sin(\varphi - \alpha)\right).$$

2) Inverse Kinematics: The inverse kinematics solves for the exoskeleton flexion angle $\varphi(\theta)$ for a desired knee flexion angle, which can be solved from (2b)

$$\varphi(\theta) = \cos^{-1}\left(\frac{(r\cos\theta + \ell_i\cos\alpha)X_O + (r\sin\theta + \ell_i\sin\alpha)Y_O}{r^2 + \ell_i^2 + 2r\ell_i\cos(\theta - \alpha)}\right). \tag{6}$$

B. Dynamic Model

The equations governing the dynamics of lower leg and link are given in (7a)–(7c) and (8a)–(8c), respectively, which provide a basis for investigating the effects of different exoskeleton designs on the internal forces and torque (f_r, f_θ, τ_a) in the knee

$$m(\ddot{r} - r\dot{\theta}^2) = mg\sin\theta + f_r + f_{er}\cos(\theta - \varphi) + f_{e\theta}\sin(\theta - \varphi) \tag{7a}$$

$$m(2\dot{r}\dot{\theta} + r\ddot{\theta}) = mg\cos\theta + f_\theta - f_{er}\sin(\theta - \varphi) + f_{e\theta}\cos(\theta - \varphi) \tag{7b}$$

$$J\ddot{\theta} + 2mr\dot{r}\dot{\theta} = \tau_g + \tau_a + \tau_e - f_{er}l\sin\gamma + f_{e\theta}l\cos\gamma \tag{7c}$$

$$m_e(\ddot{r}_e - r_e\dot{\varphi}^2) = m_e g\sin\varphi + f_l\cos\varepsilon - f_{er} - f_m\cos(\varphi + \eta) \tag{8a}$$

$$m_e(2\dot{r}_e\dot{\varphi} + r_e\ddot{\varphi}) = m_e g\cos\varphi - f_l\sin\varepsilon - f_{e\theta} + f_m\sin(\varphi + \eta) - f_d \tag{8b}$$

$$J_e\ddot{\varphi} + 2m_e r_e\dot{r}_e\dot{\varphi} = \tau_{ge} - f_{e\theta}(l_E + u) - \tau_e - \tau_m - \tau_f - \tau_l. \tag{8c}$$

The torques and moments-of-inertia in the third equations of (7) and (8) are computed about the rotation axes at C_i and C_e, respectively. For a given exoskeleton,

$$f_{er} = -k_r u - \mu f_{e\theta}\text{sign}(\dot{u}) \tag{9}$$

$$\tau_e = k_\theta(\theta_E - \theta_{E(0)}) \tag{10}$$

where $\dot{u}$ is the velocity of point E; $\theta_{E(0)}$ is the initial value of θ_E; and μ is the friction coefficient of the end slider. In (8c), τ_{ge} is the torque acting on the lower link due to gravity; τ_f

TABLE I
SPECIFICATIONS OF EXOSKELETON DESIGNS

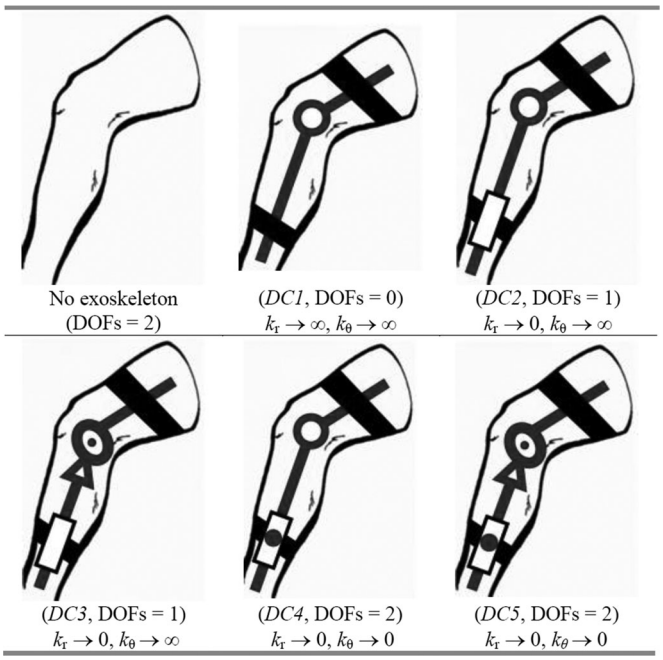

is the friction torque; (f_m, τ_m) are the actuating force/torque of the exoskeleton on the lower-link; (f_l, τ_l) are the contact force/torque of the cam roller in the cam mechanism; f_d is the contact force of the slider in cam mechanism; and the angles (ε and η) characterize the force direction of the cam-slot and motor.

III. EXPERIMENTAL INVESTIGATION

The objectives of the experimental study are 1) to validate the kinematics of the knee-exoskeleton closed-chain mechanism; 2) to analyze the tibia rolling and sliding on femur; 3) to investigate the effects of different exoskeleton design configurations on the knee internal forces and torque; and 4) to examine the feasibility of accommodating a limited range of size/shape variations with the method of adaptive knee-joint exoskeleton.

A. Design Configurations

Five design configurations (with calculated *DOFs*) along with a human knee-joint flexing freely without any exoskeleton are compared in Table I. The case without exoskeleton provides a basis for numerically investigating the effect of the exoskeleton designs on the internal forces (f_r, f_θ) and torque τ_a in the knee.

*DC*1 (Pin and fixed end): The link is connected by engineering pin-joint to the fixed brace; r_e is a constant in (8) because links are inextensible. However, these rigid links cannot adapt to the varying distance r (as has been discussed in [16], the attachment E is thus subjected to compression, extension, and torsion.

*DC*2 (Pin and slider): The link slides with respect to the leg brace to accommodate for the knee-joint translational motion in e_r direction relieving the compression at E; $k_r = 0$.

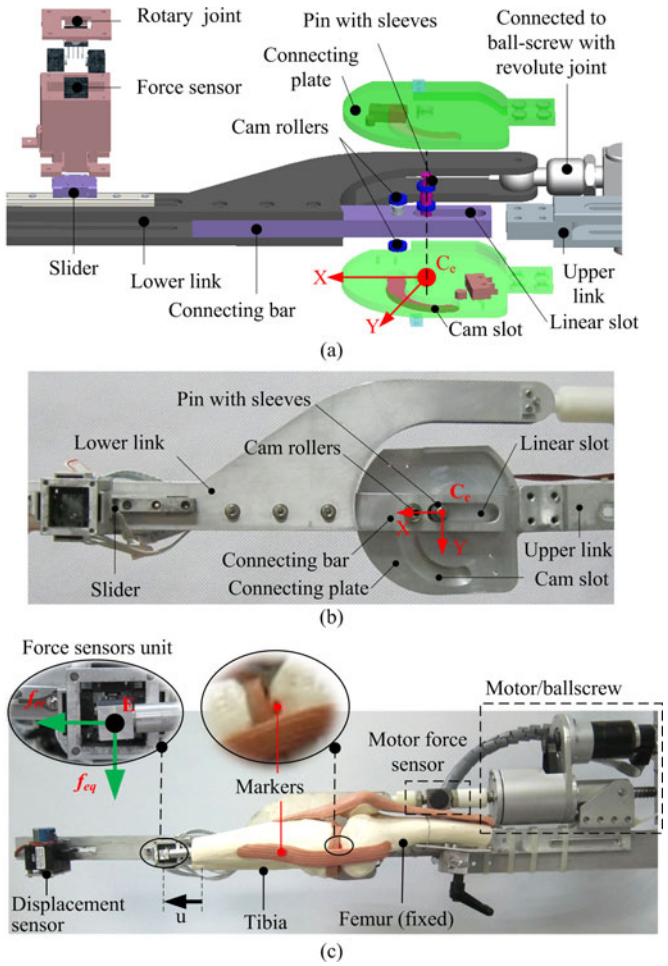

Fig. 2. Experimental setup. (a) Cam mechanism CAD exploded view. (b) Cam mechanism used in experimental setup. (c) An artificial knee joint attached on the lower-link.

*DC*3 (Cam and slider): To account for the nonuniform geometry of the biological knee joint, the hinge in *DC*2 is replaced by a grooved cam allowing the link length r_e to vary with respect to the cam profile during motion.

*DC*4 (Pin and pinned slider): The hinge in *DC*4 allows for sliding and rotating to accommodate the torque angle θ_E between the link and leg; $k_\theta = 0$ because a hinge cannot transmit torques.

*DC*5 (Cam and pinned slider): The hinge in DC5 is allowed to slide and rotate. Combined with a grooved cam, this design can accommodate changes of both the distance r and the torque angle θ_E.

B. Experimental Test Bed

Fig. 2 shows the experimental test bed built upon an existing lower extremity rehabilitation exoskeleton (LERE) [20]. As illustrated in Fig. 2(a) and (b) which shows the CAD model and the photograph of the prototype adaptive exoskeleton, respectively, the cam mechanism is made up of two assemblies which move relative to each other through a revolute joint; namely, a pair of connecting plates fixed on the upper-link at C_e (each of which has a machined slot characterizing the cam profile), and a connecting bar (with a linear slot) rigidly attached to the

lower link. As the lower link rotates, the rollers (fixed on the connecting bar) follow the slotted cam profile between the pair of connecting plates, while its cam center C_e (pin with sleeves) is allowed to slide along the linear slot of the connecting bar.

To investigate the effects of geometrical size/shape variations on the knee–exoskeleton interaction, an artificial model (A82 Functional Knee Joint Model, 3B Scientific GmbH, Germany) was chosen for emulating the knee joint mechanics in experiments as shown in Fig. 2(c). The artificial model is smaller than the human knee [17] from which the models were derived to perform hardware-in-the-loop simulation. To facilitate validation, two markers are placed at the mass-center O located experimentally and calibrated C_i for directly measuring the displacement r, the images of which can be captured with a camera for off-line analysis. A rotary joint is added at the end attachment (see point E in Fig. 1) to compensate for the angular deviation between the lower leg and the exoskeleton link. Different configurations can be investigated by engaging or disengaging some kinematic pairs. The displacement u was measured by a cable-driven potentiometer. Four force sensors (Honeywell piezo-resistive FSG-15N1 A) were used to measure f_{er} and $f_{e\theta}$.

C. Experimental Methods

In solving the kinematics and dynamics of a K-E mechanism, the point of attachment E is known. As the lower leg can be separated from the knee joint, its mass center O can be located by a force plate method [21], and thus (X_O, Y_O) can be defined after reassembly. The angle δ can be described by a polynomial function of the knee flexion angle θ [16]; for the knee joint,

$$\delta = \theta - 0.078.$$

However, the following unknowns must be calibrated.

1) Location C_i (characterized by the distance ℓ_i and angle α) which provides a basis to determine the displacement of the mass-center O as a function of flexion, $r(\theta)$.
2) Rolling/sliding displacements in the knee. These contact conditions are essential for simulating the closed kinematic chain motion of the K-E structure.
3) Design parameters of the cam profile for *DC*3 and *DC*5, which depends on specific knee size.

The calibration of the initial contact point C_i (on the femur) and the rolling/sliding displacements of the knee-joint were performed experimentally using exoskeleton *DC*4.

1) Calibration for Initial Contact Point C_i: Since $\ell_E + u$ is measurable, the X-component term of (2a) is expanded for use as a basis for calibrating ℓ_i and α

$$[\cos\varphi + \cot(\delta - \varphi)\sin\varphi]\,\ell_i\cos\alpha + [\sin\varphi - \cot(\delta - \varphi)\cos\varphi]\,\ell_i\sin\alpha = \ell_E + u. \quad (11)$$

As the K-E mechanism flexes a full range, data can be collected and organized into a system of linear equations of the form

$$[\mathbf{A}]\mathbf{Z} = \mathbf{b} \quad (12)$$

where

$$[\mathbf{A}] = \begin{bmatrix} a_{11} & a_{12} \\ \vdots & \vdots \\ a_{k1} & a_{k2} \\ \vdots & \vdots \\ a_{n1} & a_{n2} \end{bmatrix},\ [\mathbf{b}] = \begin{bmatrix} l_E + u_1 \\ \vdots \\ l_E + u_k \\ \vdots \\ l_E + u_n \end{bmatrix},\ \mathbf{Z} = \begin{bmatrix} l_i\cos\alpha \\ l_i\sin\alpha \end{bmatrix}$$

$$a_{k1} = \cos\varphi_k + \cot(\delta_k - \varphi_k)\sin\varphi_k$$

$$a_{k2} = \sin\varphi_k - \cot(\delta_k - \varphi_k)\cos\varphi_k.$$

Using a least-squares method minimizing the fitting errors, the solution to the overdetermined system (12) can be obtained from the pseudoinverse

$$\mathbf{Z} = [\mathbf{A}^{\mathrm{T}}\mathbf{A}]^{-1}\mathbf{A}^{\mathrm{T}}\mathbf{b}. \quad (13)$$

Once $\mathbf{Z}$ is solved the location C_i (l_i and α) can be calculated

$$\ell_i = \sqrt{z_1^2 + z_2^2}, \alpha = \tan^{-1}(z_2/z_1). \quad (14)$$

2) Knee Rolling/Sliding Displacements: The computation of the displacements follows three steps.

Step 1: Obtains the pure rolling distance S_p assuming that the tibia rolls purely on femur without any sliding:

$$S_p = \int \rho d\theta \quad (15)$$

where ρ is the radius of an osculating circle.

Step 2: Initializes a search point C' on the tibia that would correspond to an instantaneous C on the femur.

Step 3: Optimizes the search point C' with two constraint functions (16) along with a least-squares objective function (17) for mass-center O of the lower-leg

$$\mathbf{V}_c = \mathbf{V}_{c'} \quad \text{and} \quad C = C' \quad (16)$$

$$\mathrm{Min}\sum\{r - r_a\}^2 \quad (17)$$

where $\mathbf{V}_c$ and $\mathbf{V}_{c'}$ are the tangent vectors of the coincident points C and C', respectively; and r_a is determined by tibia position/orientation based on the chosen point C'.

With the tibia rolls and slides on the femur, the rolling distance S_r (from C_i to C on the femur, which is equal to the arc-length from C_i' to C_o on the tibia) and the sliding distance S_s (from C' to C_o on the tibia) are in analyzing the dynamics in a knee joint

$$S_r = \overset{\frown}{C_iC} \quad \text{and} \quad S_s = \overset{\frown}{C'C_o}. \quad (18)$$

3) Cam Profile Design: Modified with a scaling factor "a" and the cam-shape factor "s," the cam profile based on the model of a human knee-joint [16] for *DC*3 and *DC*5 takes the form given as

$$C_p = a\varphi(1.078\varphi^3 - 11.184\varphi^2 + 26.542\varphi - 0.825) + s. \quad (19)$$

The two design parameters (a and s) depend on knee size and shape to be determined experimentally.

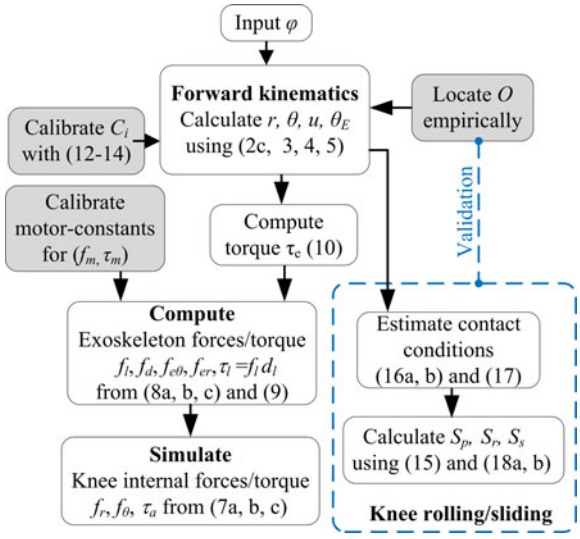

Fig. 3. Flowchart illustrating the computation of the analytical model.

TABLE II
VALUES OF PARAMETERS USED IN SIMULATION

	lower leg	Lower link	
Parameters		DC1,2,4	DC3,5
l or l_E (mm)	157.5	161	161
Effective link mass center		r_e = 158.5	r_e = 143.6
m or m_e (kg)	0.164	0.5439	0.5692
J or J_e (kg·m^2)	5.68×10^{-4}	2.069×10^{-2}	1.858×10^{-2}
Mean τ_f (N·m)	neglected	τ_f = 0.025	τ_f = 0.029
Knee joint	r_{maj} (mm)	r_{min} (mm)	
Femur	23.3	15.9	
Tibia	19.9	13	
Attachments: k_r = 8000 N/m; k_θ = 0.5 Nm/radian			
Friction coefficient, μ = 0.2			

IV. RESULTS AND DISCUSSION

The computational steps are illustrated in Fig. 3 along with the parametric values used in the simulation are listed in Table II. Since the internal knee forces and torque cannot be directly measured, they are computed from (7a)–(7c) with experimentally measured exoskeleton internal forces and torque.

Three sets of results are presented. The first set determines the values of the characteristic parameters, and validates the closed kinematic-chain model of the K-E structure by comparing the measured lower-leg mass-center displacement against the simulated result. The second set determines the rolling and sliding displacements of the knee joint. The third set investigates the effects of different exoskeleton design configurations on the knee internal forces and torque.

A. Validation of K-E Closed Kinematic-Chain Model

Using (12) to (14), the location of initial contact point C_i on the femur was experimentally calibrated on the *DC4* K-E mechanism; $\mathbf{P}_{Ci} = [X_i \ Y_i]^T$ = [3.5 6.0] in mm. The mass-center displacement $r(\theta)$ can be computed from the distance between C_i and O using (2b); the results presented by a curved-fit is given in (20a)

$$r_l = -0.80\theta^4 + 0.93\theta^3 + 6.80\theta^2 + 1.33\theta + 57.13. \quad (20a)$$

To illustrate the results and validate the models, results of (20a) are verified against two sets of data; published and experimentally measured data:

$r_s(\theta)$: published data [16] based on knee geometry scaled from a nominal model without considering the specific details of the artificial knee joint

$$r_s = a\theta(1.08\theta^3 - 11.18\theta^2 + 26.54\theta - 0.825) + 56.6. \quad (20b)$$

$r_m(\theta)$: experimental data obtained using markers placed on the lower leg and captured with a camera

$$r_m = -0.84\theta^4 + 0.83\theta^3 + 7.59\theta^2 + 1.86\theta + 56.18. \quad (20c)$$

The scaling factors in (20b) are identified to be $a = 0.6$. The results are compared in Fig. 4. All the three sets of results closely agree with each other. With the coordinate system established in this paper, full extension of a knee joint implies negative angle of the tibia orientation. The negative initial value (-5°) of the flexion angle θ (horizontal axis) is determined from the bio joint kinematic model in [16] and MRI images obtained in [17].

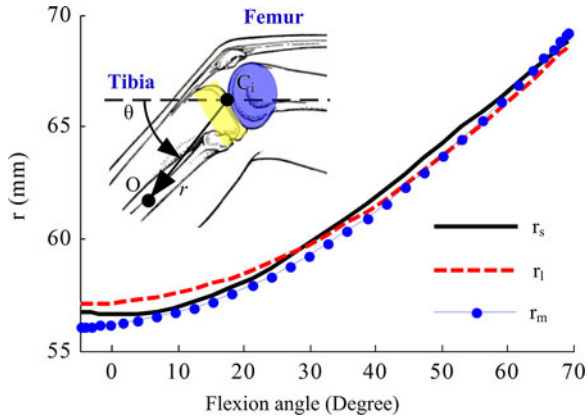

Fig. 4. Verification of computed mass-center displacements.

B. Knee Rolling/Sliding Displacement Analysis

With calibrated C_i and mass-center displacement $r_l(\theta)$, the rolling/sliding displacements (and thus the contact points C and C_i') as the tibia rolls and slides on the fixed femur are computed from (15)–(18) and simulated in Figs. 5 and 6.

Fig. 5(a) shows the calculated displacements of the lower-leg mass-center O, which agree well with measurements with an average error of 1.87 mm and a maximum difference of 2.59 mm (1.7% of the tibia length or less than 5% of the motion range). The displacements of the initial contact point C_i' (on tibia) in the y direction also agree well with experimental data in Fig. 5(b). The relative effects of the rolling and sliding as knee flexes can be analyzed in Fig. 6 showing that when $\theta < 30^\circ$, the tibia motion relative to femur is mostly rolling; after $\theta > 30^\circ$, sliding appears while rolling gradually decreases. These results, which are also consistent with the qualitative conclusion in [22]

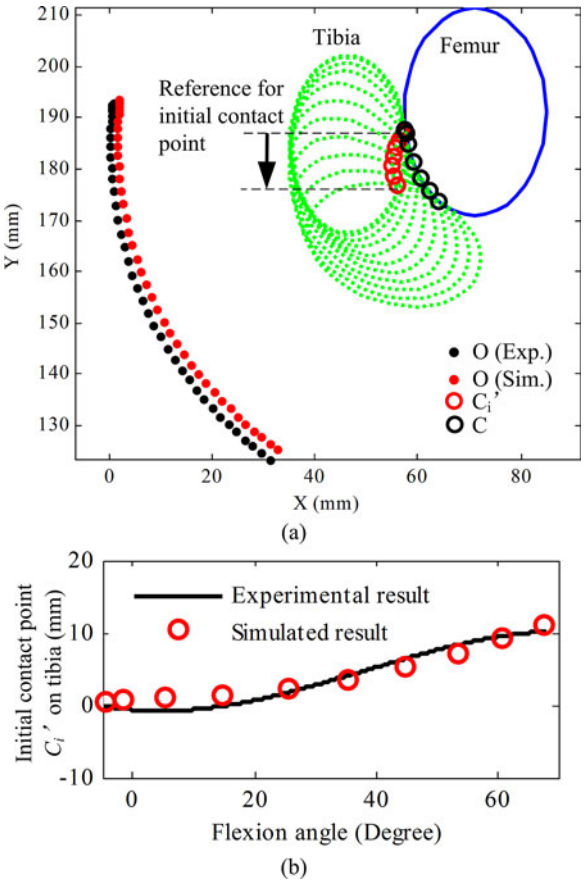

Fig. 5. Experiment and simulated contact kinematics in a knee joint. (a) Rolling/sliding and mass-center displacements. (b) Initial contact point on tibia, y-component displacement.

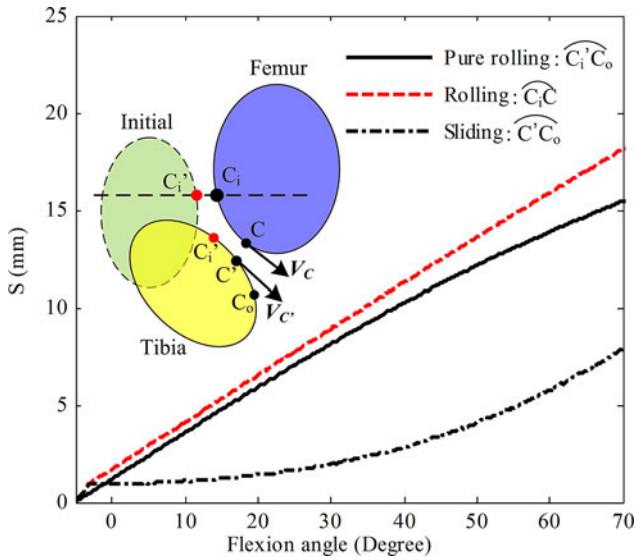

Fig. 6. Knee rolling and sliding analyses.

that rolling is dominant at the beginning of flexion, and sliding becomes dominant as knee flexes, validate the calculations of knee-joint kinematics.

C. Cam Profile Designs

The design of the cam profile has been based on two considerations. The first consideration is to account for individual size/shape variations by means of scaling and cam-shape factors based on the knee joint geometry provided in [16], [17]. The second consideration is to design the cam profile with a flat contact area (at zero flexion angle) to support the weight of the human and exoskeleton when standing. For these considerations, the effect of the correction factor "s" in (19) is analyzed by comparing two cam profiles in Fig. 7(a) against that with $s = 0$.

$C1$: $s = 25\cos(\varphi + 0.0873)$.
$C2$: $s = 15$.

The profile $C1$ is designed to accommodate the change in r due to the nonuniform geometry; while $C2$ offers similar compensation as $C1$ but includes a flat contact area at zero flexion angle to support the weight of the human and exoskeleton when standing. As compared in Fig. 7(a), $C2$ has a larger range of flatness in the neighborhood of $\varphi \in [-2^\circ, 2^\circ]$ than $C1$. The displacement u is also calculated in Fig. 7(b) based on the experimental result of r_l and (4). As shown in the aforementioned results, the cam profile $C2$ can diminish the relative motion of the exoskeleton lower link to the human lower leg, and thus chosen for the remaining research investigation and the following discussions.

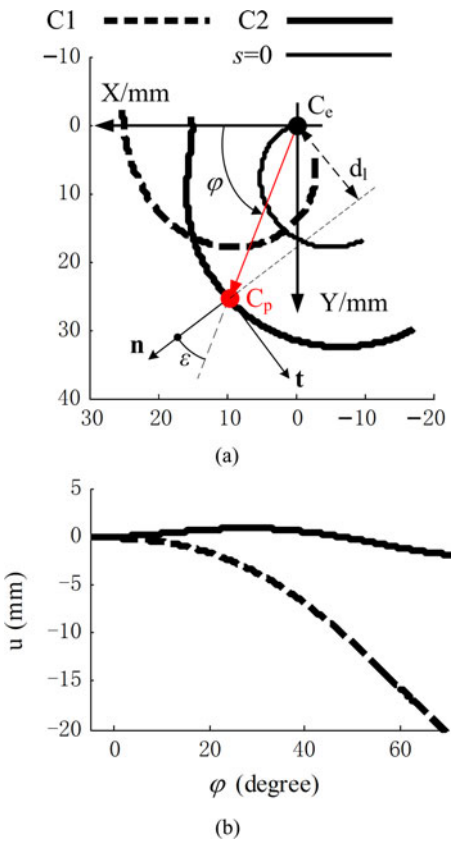

Fig. 7. Illustrative results of cam profile designs. (a) Comparison of different cam profile designs. (b) Effects of cam profiles on displacement u.

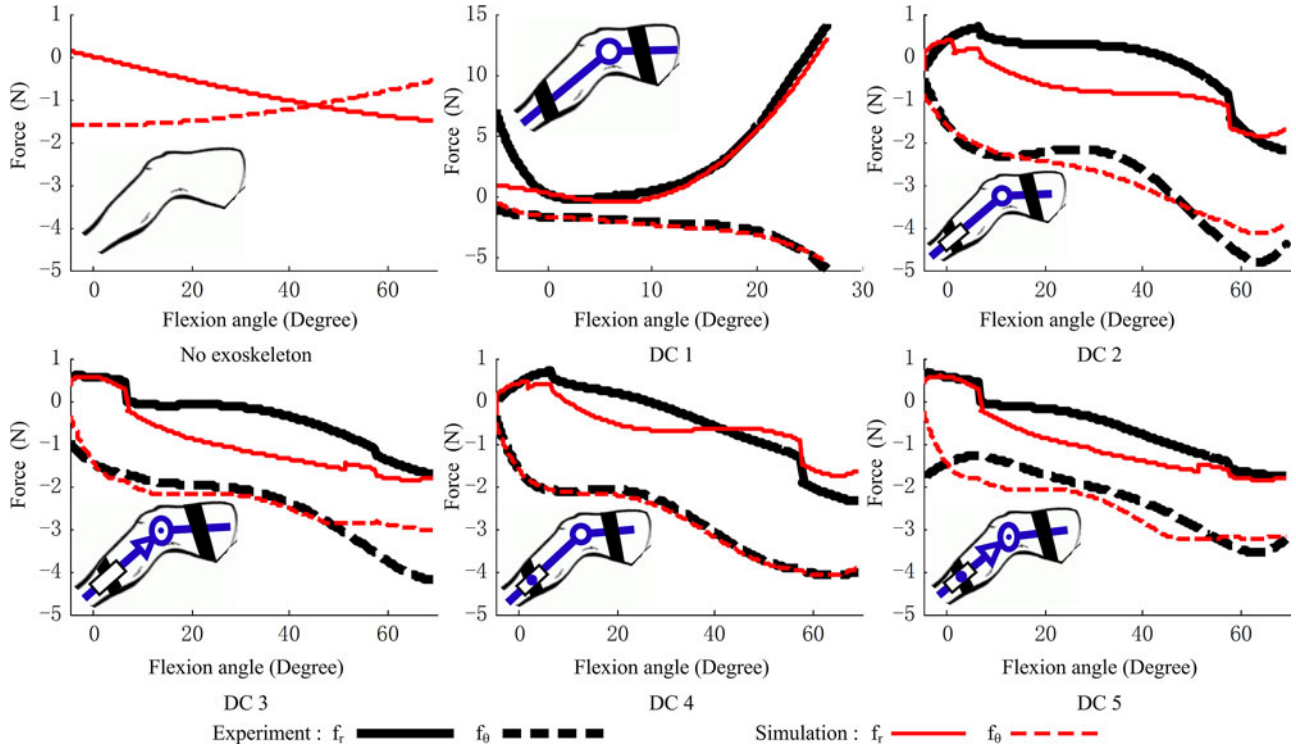

Fig. 8. Effects of different design configurations (see Table I) on human knee joint internal forces f_r , f_θ .

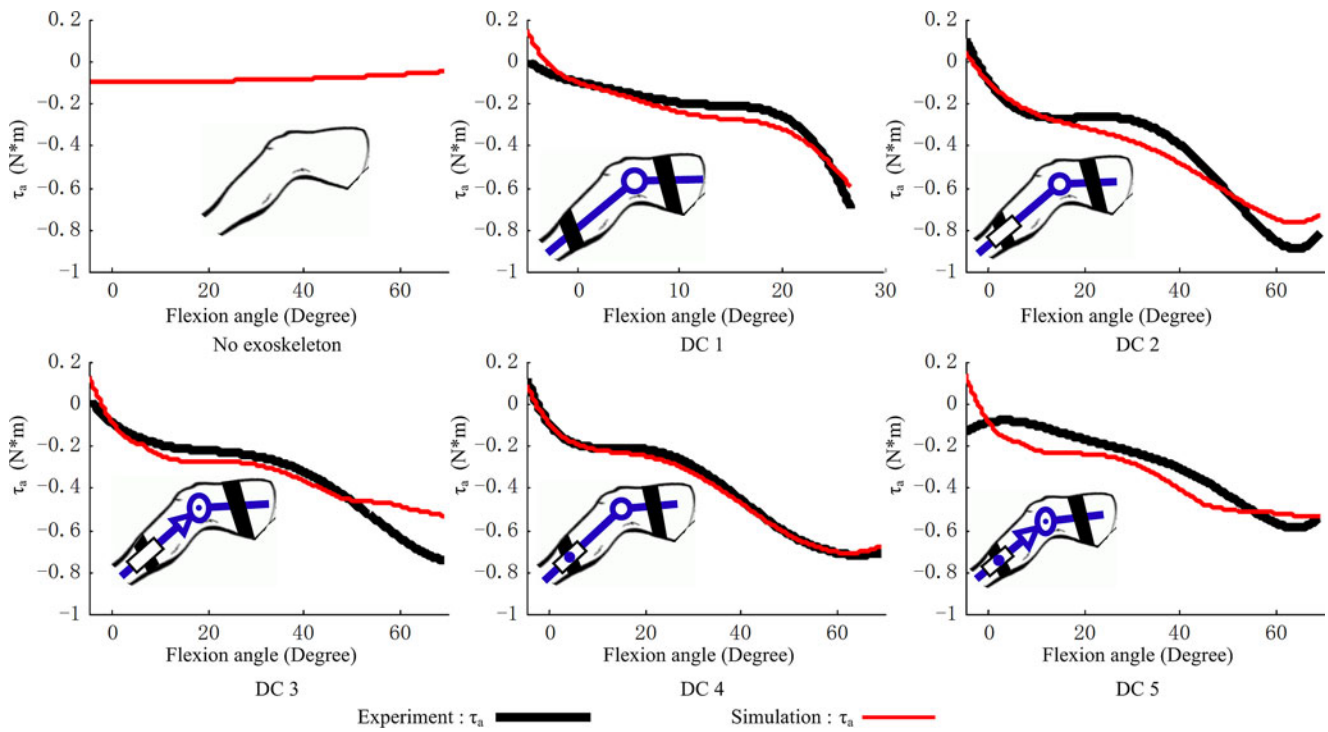

Fig. 9. Effects of different design configurations (see Table I) on human knee joint internal torque τ_a .

D. Effect of Exoskeleton on Internal Forces/Torque

Simulated and experimental results of the five design configurations are compared against the case without exoskeleton in Fig. 8, Fig. 9, and Table III where the the mean, root-mean-square (RMS), and the maximum values of the knee internal forces or torque are compared quantitatively.

Deviations between experiment and simulation results in Figs. 8 and 9 could be due to two possible causes; the mass-center location and model approximation. As compared in

TABLE III
COMPARISON OF FORCE/TORQUE (MEAN, RMS, MAX ABS VALUES)

	f_r(N)	f_θ (N)	τ_a (Nm)
Leg only	(−0.77, 0.96, 1.50)	(−1.23, 1.29, 1.61)	(−0.07, 0.08, 0.09)
DC1 (Exp)	(3.54, 5.10, 14.15)	(−2.10, 2.34, 6.00)	(−0.16, 0.22. 0.70)
(Sim)	(2.11, 3.92, 13.02)	(−2.05, 2.36, 5.29)	(−0.15, 0.24, 0.59)
DC2 (Exp)	(−0.38, 1.03, 2.17)	(−2.82, 3.10, 4.80)	(−0.41, 0.52, 0.89)
(Sim)	(−0.76, 1.04, 1.85)	(−2.80, 2.98, 4.15)	(−0.41, 0.49, 0.77)
DC3 (Exp)	(−0.42, 0.89, 1.71)	(−2.49, 2.70, 4.18)	(−0.34, 0.42, 0.74)
(Sim)	(−0.90, 1.26, 1.85)	(−2.23, 2.36, 3.03)	(−0.30, 0.35, 0.53)
DC4 (Exp)	(−0.63, 1.20, 2.37)	(−2.70, 2.93, 4.10)	(−0.37, 0.46, 0.72)
(Sim)	(−0.63, 0.95, 1.76)	(−2.75, 2.96, 4.10)	(−0.38, 0.46, 0.71)
DC5 (Exp)	(−0.57, 1.04, 1.77)	(−2.33, 2.45, 3.56)	(−0.30, 0.35, 0.58)
(Sim)	(−0.90, 1.27, 1.85)	(−2.34, 2.50, 3.24)	(−0.30, 0.37, 0.52)

Fig. 5(a), the maximum difference in the mass centers is only 1.7% of the length of tibia; this relatively small difference which may be due to measurement tolerances has little effects on the calculation of tibia dynamics. As elliptic approximation is employed for the joint geometry, the neglected higher order terms in the joint dynamics could have contributed to the deviation between experimental results and simulation in Figs. 8 and 9. Other observations providing insights into the effects of exoskeletons on the internal forces/torque in a knee-joint are summarized as follows.

The leg without exoskeleton is an open-chain mechanism, and can move freely (with low internal forces and torque experienced in the knee). Due to the directional components of the lower-leg weight, f_r becomes more negative (tensile) indicating tibia rolls and exerts normal force on femur as the knee flexes while f_θ decreases in magnitude. τ_a decreases to hold the knee in balance because of the smaller arm of gravity.

All five design configurations show that f_θ exhibits an opposite trend from the case with no exoskeleton; this is primarily because the elastic material extends beyond the artificial knee joint, and the exoskeleton exerts its own weight and actuation on the lower leg through the attachment E. In general, simulated (f_θ and τ_a) results agree well with data obtained experimentally. The discrepancies between simulated and experimental f_r suggest that nonlinear effects (such as meniscus compliance between femur and tibia) may not be neglected, and that friction in the slider and cam mechanisms is time-varying in the simulation.

With the zero-DOF *DC*1, the combined leg and exoskeleton forms an overconstrained closed-chain mechanism resulting in a significantly large compressive f_r. Simulation and experiments closely agree except near zero flexion where some discrepancies suggests a violation in the assumption that the attachment at E is linear elastic in simulation. Simulations with nonlinear stiffness k_r and k_θ could offer more realistic f_r and f_θ estimation than with the assumed linear stiffness. In practice, the attachment between the exoskeleton and leg is likely to incorporate some compliance (human skin) that would relax some internal forces but at the expense of uncomfortable slip. Because of the rigid attachment, the elastic material not only extends the artificial knee joint, but also creates the residuary flexion torque τ_e and thus a large tibiofemoral toque τ_a.

The slider in *DC*2, which offers a translational DOF along the lower link direction, greatly reduces the internal forces and torque in the knee joint, particularly, a remarkable decrease in the magnitude of f_r. As observed in the experimental results, because the cam profile was designed to adapt to the changing distance r but not the misalignment θ_E, some compressive f_r can still be observed in certain flexion angles for *DC*3. In addition, the experimental data f_θ in *DC*2 and *DC*3 are somewhat higher than the case without exoskeleton. Some discrepancies observed near final flexion angles are mainly because the nonlinear connection in attachment.

In *DC*4 and *DC*5, the added pin joint (which sets free the torque θ_E) results in smaller f_r, f_θ, and τ_a as compared to *DC*2 *and DC*3.The cam profile used in *DC*5 results in the smallest f_θ and τ_a magnitude among all design configurations. The adaptive design with slider/cam/rotary joint minimizes internal joint forces and torque due to an adaptive human-exoskeleton physical interaction.

It is worth noting that the artificial model is smaller than and does not have an identical shape as the human knee [17] from which the models were derived for simulating the human–exoskeleton interaction. Theoretically, a cam profile perfectly adaptive to the specific knee motions would be ideal. However, designing such a perfect component could be a difficult task (if not impossible). Some insights into the effect of the cam profile on the internal forces and torque of a knee joint can be gained by comparing the experimental results between the one-DOF (*DC*2*, DC*3) designs and the two-DOF (*DC*4*, DC*5) designs. With a pinned slider that set free the torque angle, the τ_a values in *DC*4 and *DC*5 are 14% and 13% lower than that in *DC*2 and *DC*3, respectively. The addition of a cam mechanism in *DC*3 and *DC*5 results in significantly reducing the forces/torque (f_r, f_θ, τ_a) magnitudes; on an average, (11%, 19%, 23%) and (12%, 17%, 23%) smaller than *DC*2 and *DC*4, respectively. Clearly, *DC*5 offers a smallest (f_θ and τ_a) magnitudes obtained experimentally than those of all other four configurations as compared in Figs. 8 and 9 and Table III. The adaptive design with the slider/cam of two DOF minimizes internal joint forces and torque due to an adaptive human–exoskeleton physical interaction. It is expected that further improvements can be made with some fine-tuning on the design of the cam profile to better match the knee joint. These encouraging experiment results, which capture the geometrical effects on the human–exoskeleton interaction, reasonably confirm that it is feasible to accommodate a limited range of individual size/shape variations (commonly encountered in real human implementation) by sizing the cam and adjusting the mechanical components of the adaptive knee joint exoskeleton.

V. CONCLUSION

By relaxing a commonly made assumption that approximates a knee joint as a perfect engineering pin-joint in exoskeleton designs, a bio-joint model is validated by the lower-leg mass-center

and used to investigate the role of adaptive kinematic components, knee rolling/sliding, and the effects of different exoskeleton designs on internal joint forces and torque.

To better understand the tibia rolling/sliding on the femur surface, a kinematic algorithm is proposed based on geometry constraint and optimization. Simulation result shows the rolling is dominant in the initial stage, and sliding becomes prevailing as the flexion increases, thus implying the necessity of adaptive knee joint designs. Five knee exoskeletons are designed with combinations of adaptive kinematic components, such as a pin, slider, and cam. Dynamic analysis is performed by comparing their performance against the case without any exoskeleton to investigate the effects of different design configurations on the joint internal forces and torque. Experimental findings suggest that incorporating a pin slider/cam can effectively minimize internal joint forces and torque from the human–exoskeleton interaction. Hence, the adaptive knee joint exoskeleton can well capture the human knee joint geometry, and minimize internal joint forces from the human–exoskeleton interaction.

ACKNOWLEDGMENT

The authors would like to thank H. Yu and S. Ma for assistance in experiments.

REFERENCES

[1] P. K. Jamwal, S. Q. Xie, S. Hussain, and J. G. Parsons, "An adaptive wearable parallel robot for the treatment of ankle injuries," *IEEE/ASME Trans. Mechatronics*, to be published, DOI: 10.1109/TMECH.2012.2219065.

[2] A. Chiri, N. Vitiello, F. Giovacchini, S. Roccella, F. Vecchi, and M. C. Carrozza, "Mechatronic design and characterization of the index finger module of a hand exoskeleton for post-stroke rehabilitation," *IEEE/ASME Trans. Mechatronics*, vol. 17, no. 5, pp. 884–894, Oct. 2012.

[3] Y. Mao and S. K. Agrawal, "Design of a cable-driven arm exoskeleton(CAREX) for neural rehabilitation," *IEEE Trans. Robot.*, vol. 28, no. 4, pp. 922–931, Aug. 2012.

[4] S. K. Banala, S. K. Agrawal, S. H. Kim, and J. P. Scholz, "Novel gait adaptation and neuromotor training results using an active leg exoskeleton," *IEEE/ASME Trans. Mechatronics*, vol. 15, no. 2, pp. 216–225, Apr. 2010.

[5] A. M. Dollar and H. Herr, "Lower extremity exoskeletons and active orthoses: challenges and state-of-the-art," *IEEE Trans. Robot.*, vol. 24, no. 1, pp. 144–158, Feb. 2008.

[6] J. J. O'Connor, T. L. Shercliff, E. Biden, and J. W. Goodfellow, "The geometry of the knee in the sagittal plane," *Proc. Inst. Mech. Eng. H*, vol. 203, pp. 223–233, 1989.

[7] J. Wismans, F. Veldpaus, J. Janssen, A. Huson, and P. Struben, "A three-dimensional mathematical model of the knee-joint," *J. Biomech.*, vol. 13, no. 8, pp. 677–685, 1980.

[8] G. Wu and P. R. Cavanagh, "ISB recommendations for standardization in the reporting of kinematic data," *J. Biomech.*, vol. 28, no. 10, pp. 1257–1261, 1995.

[9] A. H. A. Stienen, E. E. G. Hekman, F. C. T. van der Helm, and H. van der Kooij, "Self-aligning exoskeleton axes through decoupling of joint rotations and translations," *IEEE Trans. Robot.*, vol. 25, no. 3, pp. 628–633, Jun. 2009.

[10] A. Schiele and F. C. T. van der Helm, "Kinematic design to improve ergonomics in human machine interaction," *IEEE Trans. Neural Syst. Rehabil. Eng.*, vol. 14, no. 4, pp. 456–469, Dec. 2006.

[11] A. Schiele, "An explicit model to predict and interpret constraint force creation in pHRI with exoskeletons," in *Proc. IEEE Int. Conf. Robot. Autom.*, Pasadena, CA, USA, May 2008, pp. 1324–1330.

[12] A. Schiele, "Ergonomics of exoskeletons: objective performance metrics," in *Proc. 3rd Joint Eur. Conf. Symp. Haptic Interface for Virtual Environ. Teleoperator Syst.*, Salt Lake City, USA, Mar. 2009, pp. 103–108.

[13] N. Jarrasse and G. Morel, "Connecting a human limb to an exoskeleton," *IEEE Trans. Robot.*, vol. 28, no. 3, pp. 697–709, Jun. 2012.

[14] L. E. Amigo, A. Casals, and J. Amat, "Design of a 3-DoF joint system with dynamic servo-adaptation in orthotic applications," in *Proc. IEEE Int. Conf. Robot. Autom.*, Shanghai, China, May 2011, pp. 3700–3705.

[15] D. Cai, P. Bidaud, V. Hayward, and F. Gosselin, "Design of self-adjusting orthoses for rehabilitation," in *Proc. Int. Conf. Robot. Appl.*, Cambridge, MA, USA, Nov. 2009, pp. 215–223.

[16] K.-M. Lee and J. Guo, "Kinematic and dynamic analysis of an anatomically based knee joint," *J. Biomech.*, vol. 43, no. 7, pp. 1231–1236, 2010.

[17] H. Iwaki, V. Pinskerova, and M. A. R. Freeman, "Tibiofemoral movement 1: The shapes and relative movements of the femur and tibia in the unloaded cadaver knee," *J. Bone Joint Surg.*, vol. 82-B, no. 8, pp. 1189–1195, 2000.

[18] V. V. Pate1, K. Hall, M. Ries, J. Lotz, E. Ozhinsky, C. Lindsey, Y. Lu, and S. Majumdar, "A three-dimensional MRI analysis of knee kinematics," *J. Orthopaedic Res.*, vol. 22, no. 2, pp. 283–292, 2004.

[19] D.-H. Wang, J. Guo, K.-M. Lee, C.-J. Yang, and H. Yu, "An adaptive knee joint exoskeleton based on biological geometries," in *Proc. IEEE Int. Conf. Robot. Autom.*, Shanghai, China, May 2011, pp. 1386–1391.

[20] J.-F. Zhang, Y.-m. Dong, C.-j. Yang, Y. Geng, Y. Chen, and Y. Yang, "5-Link model based gait trajectory adaption control strategies of the gait rehabilitation exoskeleton for post-stroke patients," *Mechatronics*, vol. 20, no. 3, pp. 368–376, 2010.

[21] M. Damavandi, N. Farahpour, and P. Allard, "Determination of body segment masses and centers of mass using a force plate method in individuals of different morphology," *Med. Eng. Phys.*, vol. 31, no. 9, pp. 1187–1194, 2009.

[22] Z.-K. Ling, H.-Q. Guo, and S. Boersma, "Analytical study on the kinematic and dynamic behaviors of a knee joint," *Med. Eng. Phys.*, vol. 19, no. 1, pp. 29–36, 1997.

Donghai Wang received the B.Eng. degree from the Department of Mechanical Engineering, Zhejiang University, Hangzhou, China, in 2010. He is currently working toward the Ph.D. degree in the State Key Laboratory of Fluid Power Transmission and Control, Zhejiang University.

His current research interests include rehabilitation robots and bio-inspired exoskeleton joints.

Kok-Meng Lee (M'89–SM'02–F'05) received the B.S. degree from the State University of New York, Buffalo, NY, USA, in 1980, and the S.M. and Ph.D. degrees from the Massachusetts Institute of Technology, Cambridge, MA, USA, in 1982 and 1985, respectively.

He is currently a Professor in the George W. Woodruff School of Mechanical Engineering at the Georgia Institute of Technology, Atlanta, GA, USA. He was also honored as Pao Yu-Kong Chair Professor at Zhejiang University. He is also a Distinguished Professor with the State Key Laboratory of Digital Manufacturing Equipment and Technology at Huazhong University of Science and Technology, Wuhan, China, under the National Recruitment Program of Global Experts. He holds eight patents in machine vision, a three degrees of freedom (DOF) spherical motor/encoder, and a live-bird handling system. His research interests include system dynamics/control, robotics, automation, and mechatronics.

Dr. Lee is a Fellow of the American Society of Mechanical Engineers (ASME). He received the National Science Foundation (NSF) Presidential Young Investigator, Sigma Xi Junior Faculty Research, International Hall of Fame New Technology, and Kayamori Best Paper Awards.

Jiajie Guo (M'10) received the B.S. degree from the Department of Engineering Mechanics and Science, Peking University, Beijing, China, in 2006, and the M.S. and Ph.D. degrees in mechanical engineering from the Georgia Institute of Technology, Atlanta, GA, USA, in 2009 and 2011, respectively.

He is currently an Associate Professor in the School of Mechanical Science and Engineering, Huazhong University of Science and Technology, Wuhan, China. His current research interests include compliant mechanisms, mechatronics, and system dynamics/control.

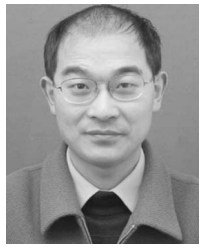

Can-Jun Yang received the B.Eng. and M.Eng. degrees from Nanjing University of Aeronautics and Astronautics, Nanjing, China, in 1991 and 1994, respectively, and the Ph.D. degree from Zhejiang University, Hangzhou, China, in 1997.

Since 1997, he has been with Zhejiang University, where he is currently a Professor in the State Key Laboratory of Fluid Power Transmission and Control, and a member of the National Industrial Technological Innovation Union Council for Rehabilitation Technical Aids. His current research interests include man–machine intelligent mechatronic systems and deep-sea mechatronic equipment techniques.

Dr. Yang received the 2nd Prize of the National Award for Technical Invention in 2009.